Autonomous Inductive Power Transfer System With Quasi Constant Power Output Against Coupling and Load Variations

Aoyang Laurence Li, *Student Member, IEEE*, Mingdong Edward Han, *Student Member, IEEE*, Saidul Alam Chowdhury, and Aiguo Patrick Hu, *Senior Member, IEEE*

***Abstract*—The output power of an inductive power transfer (IPT) system may fluctuate with magnetic coupling and load variations. Traditional methods of achieving constant output power require dedicated power regulation by complex feedback control based on communication between the power transmitter (Tx) and receiver (Rx). This article presents a communication free autonomous voltage-fed inverter (AVFI) for a series–series compensated IPT system to achieve a constant wireless power output against magnetic coupling and load variations. A synchronized gate control method is proposed by following the zero crossings of the induced voltage of the Tx current. A thorough theoretical study is conducted to analyze the steady-state operation of the system. A 65 W prototype is built, and the experimental results show that the proposed AVFI system can deliver quasi constant power with a maximum 10% fluctuation when the coupling coefficient and the load are varied from 0.2 to 0.6 and 14 to 26 Ω, respectively.**

***Index Terms*—Autonomous inverter, constant power (CP), inductive power transfer (IPT).**

I. INTRODUCTION

INDUCTIVE power transfer (IPT) systems offer several advantages over equivalent conventional direct electrical contact systems [1], [2]. Due to the nature of IPT applications, a battery inside the receiving device is usually the load. Traditionally, battery charging involves a constant current (CC) stage followed by a constant voltage stage [3]. However, replacing the CC stage with a constant power (CP) stage can improve charging speed and battery health [4], ultimately minimizing charge time as it utilizes the maximum power transfer capacity of the charger [5].

CP delivery is utilized in applications such as battery chargers [6], [7], drones [8], [9]. However, it is very difficult to maintain CP because the magnetic field coupling and load variations of an IPT system have significant effects. Solutions have been proposed to counter these challenges based on control algorithms, power estimation, and Tx–Rx communication to maintain CP. From the literature, IPT systems that achieve CP are generally categorized into the following three types:

1) both primary and secondary side control;
2) secondary side control;
3) primary side control.

Both primary and secondary side control work together to achieve CP in [10]. Specifically, CP is achieved by controlling the conduction angle of the inverter and active rectifier, coordinated through RF wireless communication to adjust the phase shift angle. While effective, this approach requires communication modules, which add components and pose risks in case of communication failure. In [11], an LCC–LCC topology with a switch-controlled capacitor (SCC) on both the primary and secondary achieves CP without wireless communication. However, the work in [11] requires additional capacitors, switches and complex control, increasing system size, cost and power loss.

Secondary side control involves adjusting parameters on the receiver side, such as the load impedance, rectifier settings, or additional reactive components to regulate the power drawn from the primary side. The constant output power is achieved in [12] and [13] by controlling an SCC and semi-active rectifier to manipulate the impedance of the receiver side. In [14], an LCC-S topology uses only a semi-active rectifier with pulse-density-modulation control. However, the main drawback of [12], [13], [14] is that they require additional circuit components, increasing the size and weight of the receiving device. Moreover, they need complex PI control to adjust the output power. In addition, the method in [13], requires wireless communication as the controller on the secondary side requires primary side current information.

Primary side control includes methods based on parameter estimations using primary side information [15], [16], [17], [18], [19] and parity-time (PT) [8], [9], [20], [21], [22], [23]. The methods in [15], [16], [17], [18], and [19] are capable of estimating output power. However, achieving power regulation often necessitates additional components, primarily a dc–dc converter, which can impact system size and cost. In [15], a complex estimation algorithm is required, while paper [16] employs offline estimation. In [17], mutual inductance and load are determined using an adaptive differential evolution algorithm, and in [18], a pulse density modulation inverter generates and utilizes the inter-harmonics for estimation. However, for papers

---

Received 6 February 2025; revised 20 March 2025; accepted 15 April 2025. Date of publication 2 May 2025; date of current version 30 June 2025. Recommended for publication by Associate Editor Y. Tang. *(Corresponding author: Aiguo Patrick Hu.)*

The authors are with the Department of Electrical, Computer and Software Engineering, The University of Auckland, Auckland 1023, New Zealand (e-mail: ali080@aucklanduni.ac.nz; mhan937@aucklanduni.ac.nz; saidul.chowdhury@auckland.ac.nz; a.hu@auckland.ac.nz).

Color versions of one or more figures in this article are available at https://doi.org/10.1109/TPEL.2025.3564913.

Digital Object Identifier 10.1109/TPEL.2025.3564913

TABLE I
COMPARISON BETWEEN THE PROPOSED AND EXISTING METHODS

Reference	Method	Additional Power Components	Tx–Rx Communication	Control Requirement	Increase Rx Size
[10]	Active rectifier	No	Yes	Complex control algorithm	Yes
[14]			No	Complex PI	
[11]	SCC + Active rectifier	2 capacitors, 4 switches			
[12]		1 capacitor, 2 switches			
[13]			Yes		
[15], [16], [17], [18], [19]	Parameter estimation	1 dc-dc converter	No		No
[22]	Parity-time				
[23]		Phase shift inverter			
This article	Proposed AVFI	No		No	

[17] and [18], the computation time for each estimation is long. In [19], mutual inductance and load are estimated by adding an SCC to the primary side. However, this method requires switching the capacitors for each estimation, which disrupts power transfer.

The methods proposed in [8], [9], [20], [21], [22], and [23] achieve CP based on PT symmetry-based systems. They utilize a negative resistance element on the primary side to self-adjust the operating frequency. In [8], [9], [20], and [21], CP is achieved at the output of the IPT system across a range of distances, but the variation of load resistance is not considered. Although the load resistance change is addressed in [22] and [23]. The drawback of [22] is that it requires a front-end dc–dc converter and complex PI control to regulate the output power. In [23], a phase-shifted inverter is used to control the output power. However, switching losses occur in a phase-shifted inverter as the load and coupling change. Additionally, [23] relies on complex PI-based control and uses a large receiver coil (520 μH), which is impractical for certain applications. While the methods in [9], [10], [11], [12], [13], [14], [15], [16], [17], [18], [19], [20], [21], [22], and [23] present their own challenges, the self-oscillating inverters proposed in the literature [24], [25], [26] also face limitations, as they do not achieve CP against coupling and load variations. Table I compares the existing works that deliver CP against both coupling and load variations with the proposed.

This article proposes a simple SS compensated IPT system with an autonomous voltage-fed inverter (AVFI) that delivers quasi CP against coupling and load variations, by switching the inverter at the zero-crossing of the induced voltage from the transmitter (Tx) current, which aligns with the peak of the Tx current. The advantages and contributions of the proposed AVFI system in this article are summarized as follows.

1) The IPT system with the proposed AVFI achieves CP against coupling and load variations at fixed dc input voltage, thus dc–dc converter or control algorithm is not required, unlike [10], [12], [13], [14], [15], [16], [17], [18], [19] and [22], [23].
2) The proposed AVFI method does not need additional power components, unlike [11], [12], [13] and [15], [16], [17], [18], [19], [20], [21], [22], [23]. Therefore, the IPT system size, power loss and cost are kept low.
3) The proposed AVFI IPT system does not require communication between the primary and secondary sides, unlike [10] and [13], thus improving robustness by avoiding issues associated with communication.

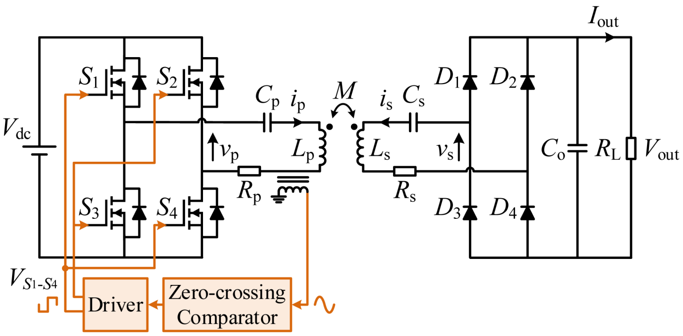

Fig. 1. Schematic of the proposed AVFI system.

II. PROPOSED SYSTEM MODELLING AND ANALYSIS

The proposed AVFI IPT system to achieve CP is shown in Fig. 1. This work utilizes a full bridge inverter with switches S_1–S_4 on the primary side, converting the input dc voltage V_{dc} into an ac square wave v_{p}. On the secondary side, a full bridge diode rectifier D_1–D_4 produces the dc output voltage V_{out} with output current I_{out}. The primary and secondary coils have self-inductances L_{p} and L_{s}, with equivalent series resistance R_{p} and R_{s}, respectively. The mutual inductance between L_{p} and L_{s} is denoted as M. The coupling coefficient k is a function of M as $k = M \,/\sqrt{L_{\mathrm{p}}L_{\mathrm{s}}}$. The C_{p} and C_{s} are the compensation capacitors for L_{p} and L_{s}. The primary and secondary currents flowing through L_{p} and L_{s} are represented by i_{p} and i_{s}. C_{o} is the output filter capacitor, and R_{L} is the load resistance. The equivalent circuit is shown in Fig. 2(a), where $R_{\mathrm{eq}} = 8R_{\mathrm{L}}/\pi^2$ represents the equivalent load resistance.

The proposed AVFI operates the full bridge inverter using a 50% duty cycle signal synchronized with the zero-crossing

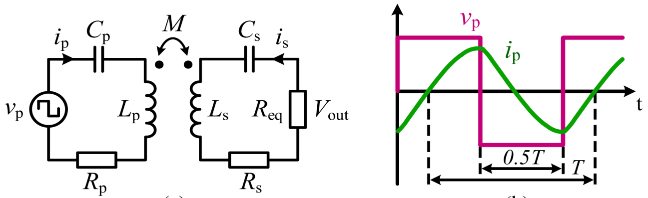

(a) (b)

Fig. 2. Proposed AVFI IPT system. (a) Equivalent circuit. (b) Operating waveforms showing inverter voltage v_{p}, and primary current i_{p}, at steady state.

of the induced voltage of the Tx current. This principle results in autonomous adjustment of the operating frequency such that quasi CP is achieved against coupling and load variations. Time domain and Laplace domain methods are employed to analyze the transient behavior of the system, while frequency domain analysis focuses on its steady-state operation.

A. Analysis of Steady-State Operating Frequency for the Proposed AVFI

The proposed AVFI operates by switching at the zero-crossing of the induced voltage from the Tx current, which aligns with the peak of the primary current i_{p} as shown in Fig. 2(b). This principle is used to determine the proposed system steady-state operating frequency. The relationship arises from the fact that the voltage across an inductor in the time domain acts as a differentiator, which means the voltage becomes zero when the current reaches its peak, as expressed

$$v_{\mathrm{L}}(t) = L\frac{di(t)}{dt}. \tag{1}$$

The time it takes to reach the peak of the primary current depends on the system parameters and initial conditions, which inherently determines the steady-state operating frequency of the proposed AVFI. A detailed analysis of the transient period is required to determine the steady-state operating frequency, with particular attention to the dynamic behavior of the inverter during each switching cycle. Fig. 3 outlines the procedure to identify the steady-state system operating frequency.

First, apply Kirchhoff's voltage law to the equivalent circuit in Fig. 2(a), and then take the time domain response

$$v_{\mathrm{p}}(t) = L_{\mathrm{p}}\frac{di_{\mathrm{p}}(t)}{dt} + R_{\mathrm{p}}i_{\mathrm{p}}(t) + \frac{1}{C_{\mathrm{p}}}\int i_{\mathrm{p}}(t)\,dt + M\frac{di_{\mathrm{s}}(t)}{dt} \tag{2}$$

$$L_{\mathrm{s}}\frac{di_{\mathrm{s}}(t)}{dt} + (R_{\mathrm{s}} + R_{\mathrm{eq}})\,i_{\mathrm{s}}(t) + \frac{1}{C_{\mathrm{s}}}\int i_{\mathrm{s}}(t)\,dt + M\frac{di_{\mathrm{p}}(t)}{dt} = 0 \tag{3}$$

where (2) is the primary circuit and (3) is the secondary circuit in the time domain. Next, convert to the Laplace domain considering the initial conditions and a step input

$$V_{\mathrm{p}}(s) = \frac{\pm V_{\mathrm{dc}}}{s} = \left(L_{\mathrm{p}}s + R_{\mathrm{p}} + \frac{1}{C_{\mathrm{p}}s}\right) I_{\mathrm{p}}(s) + MsI_{\mathrm{s}}(s) - L_{\mathrm{p}}I_{\mathrm{p},0} - MI_{\mathrm{s},0} + \frac{V_{\mathrm{Cp},0}}{s} \tag{4}$$

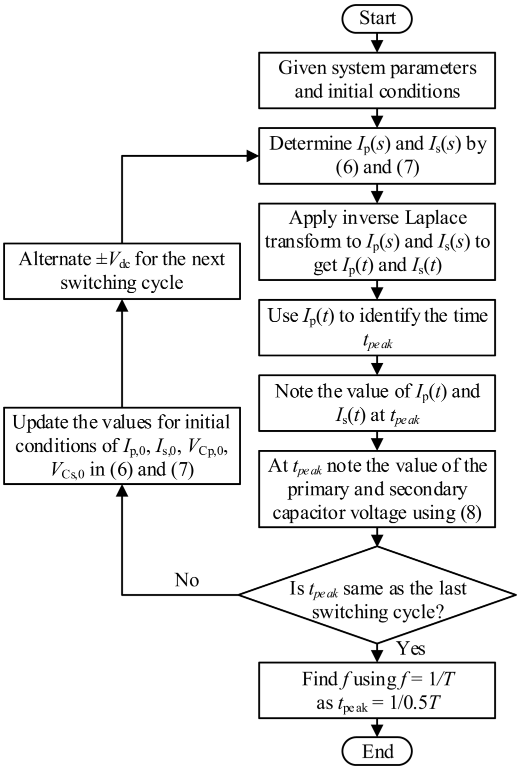

Fig. 3. Steady-state system operating frequency f identification procedure.

$$\left(L_{\mathrm{s}}s + (R_{\mathrm{s}} + R_{\mathrm{eq}}) + \frac{1}{C_{\mathrm{s}}s}\right) I_{\mathrm{s}}(s) + MsI_{\mathrm{p}}(s) - L_{\mathrm{s}}I_{\mathrm{s},0} - MI_{\mathrm{p},0} + \frac{V_{\mathrm{Cs},0}}{s} = 0 \tag{5}$$

where (4) is the primary circuit and (5) is the secondary circuit in the Laplace domain, $I_{\mathrm{p},0}$ and $I_{\mathrm{s},0}$ are the initial current through the primary inductor L_{p} and secondary inductor L_{s}, respectively, and $V_{\mathrm{Cp},0}$ and $V_{\mathrm{Cs},0}$ are the initial voltage across the primary capacitor C_{p} and secondary capacitor C_{s}, respectively. The output of an inverter is a square wave, and for a full-bridge inverter, the magnitude is equal to the inverter input dc voltage V_{dc}. A square wave in the Laplace domain can be analyzed as a step input $V(s) = \pm V_{\mathrm{dc}}/s$ that cycles between positive and negative magnitude.

Combing and rearranging (4) and (5) an expression for current $I_{\mathrm{p}}(s)$ and $I_{\mathrm{s}}(s)$ can be obtained

$$I_{\mathrm{p}}(s) = \frac{\frac{\pm V_{\mathrm{dc}}}{s} - \frac{V_{\mathrm{Cp},0}}{s} + I_{\mathrm{p},0}\,L_{\mathrm{p}} + I_{\mathrm{s},0}\,M - \frac{C_{\mathrm{s}}\,M\,s\,(I_{\mathrm{s},0}\,L_{\mathrm{s}}\,s - V_{\mathrm{Cs},0} + I_{\mathrm{p},0}\,M\,s)}{C_{\mathrm{s}}\,L_{\mathrm{s}}\,s^2 + C_{\mathrm{s}}\,(R_{\mathrm{s}} + R_{\mathrm{eq}})\,s + 1}}{R_{\mathrm{p}} + L_{\mathrm{p}}\,s + \frac{1}{C_{\mathrm{p}}\,s} - \frac{C_{\mathrm{s}}\,M^2\,s^3}{C_{\mathrm{s}}\,L_{\mathrm{s}}\,s^2 + C_{\mathrm{s}}\,(R_{\mathrm{s}} + R_{\mathrm{eq}})\,s + 1}} \tag{6}$$

$$I_{\mathrm{s}}(s) = \frac{\frac{V_{Cs,0}}{s} - I_{\mathrm{s},0}L_{\mathrm{s}} - I_{\mathrm{p},0}M + I_{\mathrm{p}}(s)Ms}{(R_{\mathrm{s}} + R_{\mathrm{eq}}) + L_{\mathrm{s}}s + \frac{1}{C_{\mathrm{s}}s}}. \tag{7}$$

Next, the inverse Laplace transform is applied to (6) and (7) to obtain the time domain expressions. Mathematical tools such

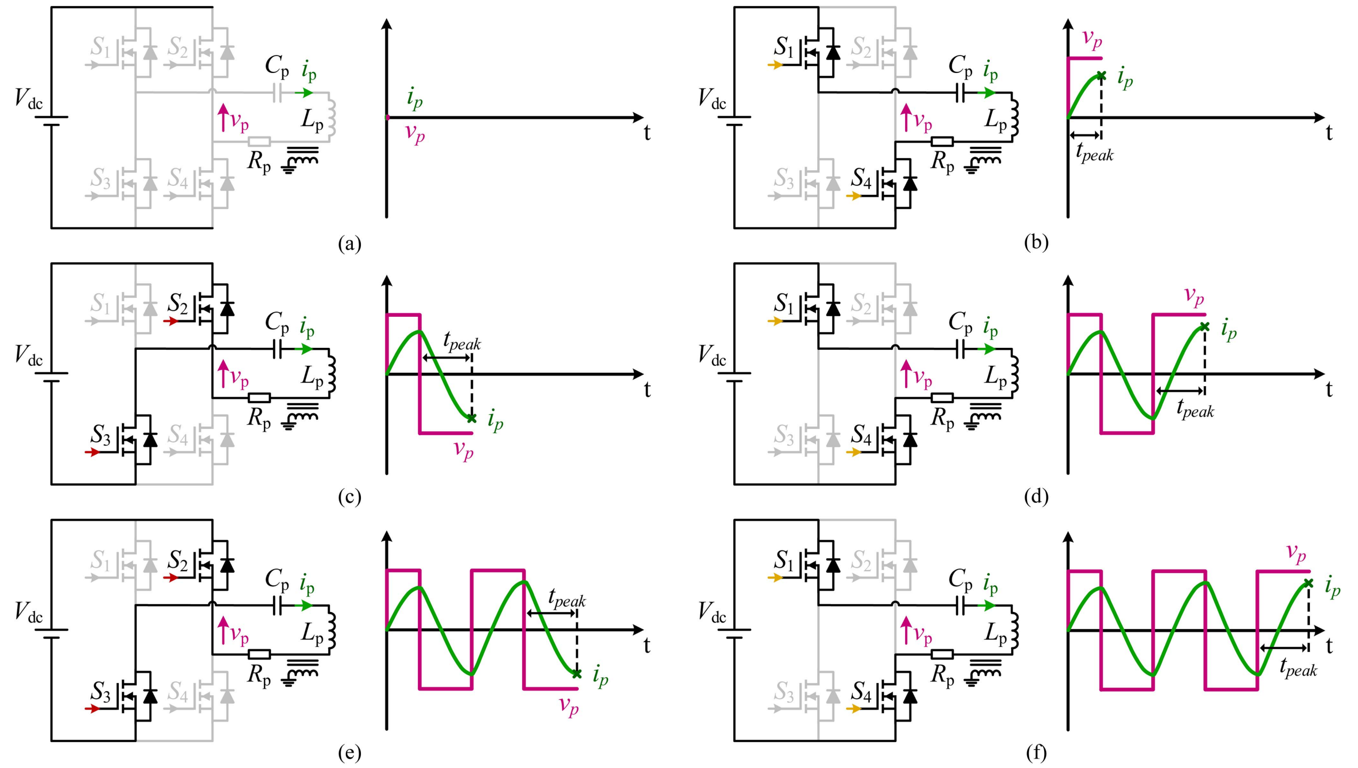

Fig. 4. Individual switching cycle waveforms of the proposed AVFI inverter. (a) Prior to startup. (b) First switching cycle. (c) Second switching cycle. (d) Third switching cycle. (e) Fourth switching cycle. (f) Fifth switching cycle.

as MATLAB or Mathematica can be used to find a solution. Due to the length and complexity of the time domain expression, a general expression for $i_\mathrm{p}(t)$ and $i_\mathrm{s}(t)$ are given in the Appendix.

With the time domain equation for current $i_\mathrm{p}(t)$, identify and record the time t_peak when the first peak current occurs relative to the instant when the inverter output voltage v_p transitions between positive and negative magnitudes. Next, note the value of the current through the inductors L_p and L_s at t_peak which correspond to $I_{\mathrm{p},0}$ and $I_{\mathrm{s},0}$ as well as the corresponding voltage across capacitors C_p and C_s which correspond to $V_{\mathrm{Cp},0}$ and $V_{\mathrm{Cs},0}$. Below is the general Laplace domain equation for the voltage across a capacitor

$$V_\mathrm{C}(s) = \frac{I(s)}{sC} - \frac{V_0}{s} \tag{8}$$

where $I(s)$ is the current through the capacitor and V_0 is the initial voltage across the capacitor.

After analyzing the circuit response to a positive step input and determining the voltage across the capacitors C_p and C_s and the current through the inductors L_p and L_s, update the initial conditions in (6) and (7) for the next inverter switching cycle (a negative step input) and reanalyze up to (7).

Fig. 4 illustrates individual switching cycle waveforms of the proposed AVFI inverter. By analyzing each switching cycle individually, where the step input alternates between positive and negative magnitude, the steady-state operating frequency is deduced by monitoring the time t_peak. As the system enters steady-state operation, the time t_peak becomes constant. The number of switching cycles the system requires before entering steady-state depends on the circuit parameters. At steady-state, the time the t_peak occurs represents half a period $t_\mathrm{peak} = 0.5T$. Therefore, given the t_peak, the operating frequency $f = 1/T$ is then calculated.

Using the parameters in Table II and the theoretical method presented in this section, Fig. 5(a) shows the theoretical and simulation results for the steady-state operating frequency, with the simulations conducted using PSIM software. The results indicate that the operating frequency varies with coupling and load variations due to switching at peak primary current. The method presented in this section effectively determines the steady-state operating frequency of the proposed system.

B. Analysis of Steady-State Output Power

Using the method presented in Section II-A to find the steady-state operating frequency, commonly used frequency domain analysis for an SS IPT system is then employed to find the dc output voltage, current, and output power at steady-state. Using the equivalent circuit shown in Fig. 2(a), the dc output current I_out and voltage V_out is derived as follows

$$I_\mathrm{out} = \frac{2\sqrt{2}\omega M V_\mathrm{p}}{\pi\sqrt{\left[R_\mathrm{p}(R_\mathrm{s}+R_\mathrm{eq})-X_\mathrm{p}X_\mathrm{s}+(\omega M)^2\right]^2+\left[X_\mathrm{s}R_\mathrm{p}+X_\mathrm{p}(R_\mathrm{s}+R_\mathrm{eq})\right]^2}} \tag{9}$$

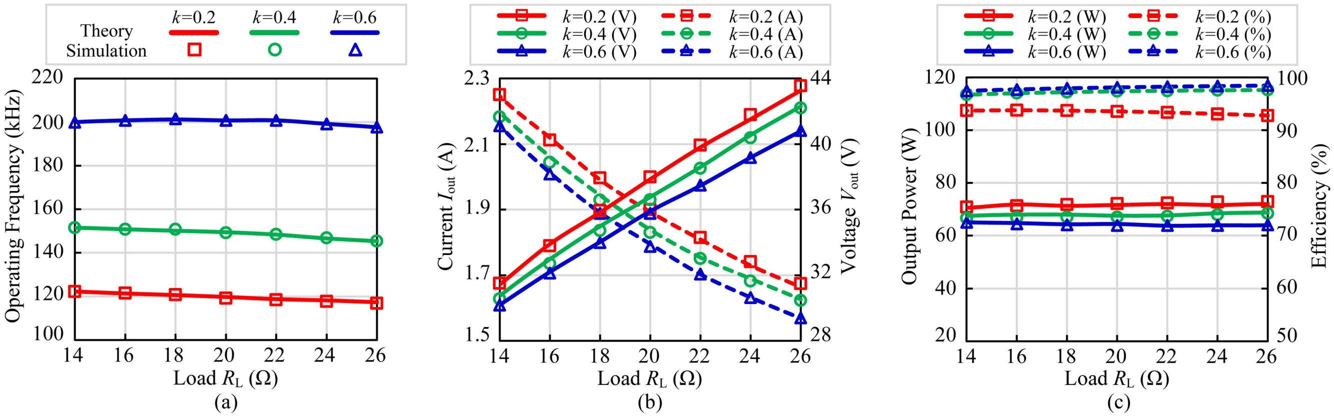

(a) (b) (c)

Fig. 5. Theoretical and simulation results at different coupling coefficient and load. (a) Steady-state operating frequency. (b) Output current I_{out} and voltage V_{out}. (c) Output power and efficiency.

$$V_{\mathrm{out}} = \frac{\pi \omega M V_{\mathrm{p}} R_{\mathrm{eq}}}{2\sqrt{2}\sqrt{\left[R_{\mathrm{p}}(R_{\mathrm{s}}+R_{\mathrm{eq}})-X_{\mathrm{p}}X_{\mathrm{s}}+(\omega M)^2\right]^2+\left[X_{\mathrm{s}}R_{\mathrm{p}}+X_{\mathrm{p}}(R_{\mathrm{s}}+R_{\mathrm{eq}})\right]^2}}. \tag{10}$$

From (9) and (10), the output power P_{out} can be deduced

$$P_{\mathrm{out}} = \frac{(\omega M)^2 V_{\mathrm{p}}^2 R_{\mathrm{eq}}}{\left[R_{\mathrm{p}}\left(R_{\mathrm{s}}+R_{\mathrm{eq}}\right)-X_{\mathrm{p}}X_{\mathrm{s}}+(\omega M)^2\right]^2+\left[X_{\mathrm{s}}R_{\mathrm{p}}+X_{\mathrm{p}}\left(R_{\mathrm{s}}+R_{\mathrm{eq}}\right)\right]^2} \tag{11}$$

where

$$\begin{cases} X_{\mathrm{p}} = \omega L_{\mathrm{p}} - \frac{1}{\omega C_{\mathrm{p}}} \quad X_{\mathrm{s}} = \omega L_{\mathrm{s}} - \frac{1}{\omega C_s} \\ M = k\sqrt{L_{\mathrm{p}}L_{\mathrm{s}}} \\ \omega = 2\pi f. \end{cases} \tag{12}$$

Additionally, ac–ac efficiency of the equivalent circuit shown in Fig. 2(a), it is expressed as follows [27]

$$\eta = \frac{(\omega M)^2 R_{\mathrm{eq}}}{R_{\mathrm{p}}\left[\left(R_{\mathrm{s}}+R_{\mathrm{eq}}\right)^2+{X_{\mathrm{s}}}^2\right]+(\omega M)^2\left(R_{\mathrm{s}}+R_{\mathrm{eq}}\right)}. \tag{13}$$

From (11), the output power expression includes the load resistance, mutual inductance and angular frequency. However, as analyzed in Section II-A, the operating frequency varies with magnetic coupling and load variations, so (11) is not a full closed form expression. Using the parameters in Table II and the steady-state operating frequency results from Fig. 5(a), the output current I_{out} and voltage V_{out} are calculated using (9) and (10) presented in Fig. 5(b), and the output power P_{out} and efficiency, calculated using (11) and (13) are shown in Fig. 5(c). The results show that the output current of the proposed system decreases with the increase of the output voltage, leading to a quasi constant output power.

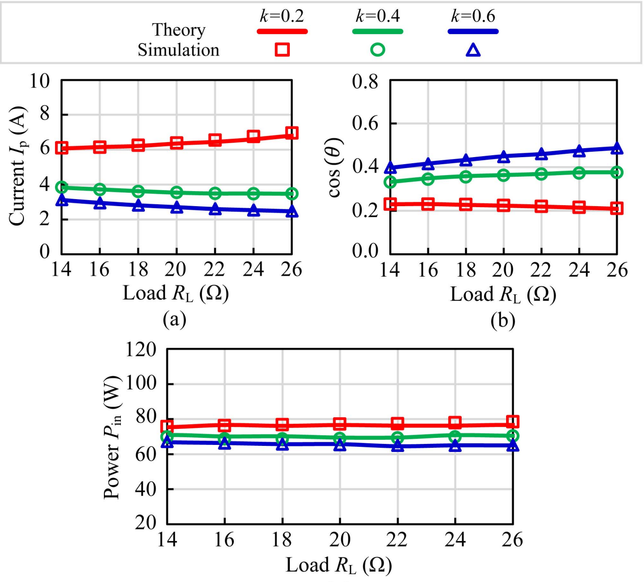

(a) (b) (c)

Fig. 6. Theoretical and simulation results of the system at different coupling coefficient and load. (a) Current I_{p}. (b) Cosine of phase. (c) Power P_{in}.

C. Alternative Analysis of Steady-State Output Power

To explain why the system output power is kept approximately constant against the load and coupling variations, the following input power equation is used to analyze the general power flow:

$$P_{\mathrm{in}} = V_{\mathrm{p}}\, I_{\mathrm{p}} \cos(\theta) \tag{14}$$

where V_{p} and I_{p} are the fundamental RMS voltage and current at the input of Tx, and θ is the phase angle between them. The fundamental input voltage V_{p} is constant with a given dc input voltage to the proposed system. The phase angle θ is derived from the input impedance, and for the equivalent circuit in Fig. 2(a), it is expressed as follows [28]

$$\theta = \tan^{-1}\left(\frac{X_{\mathrm{in}}}{R_{\mathrm{in}}}\right) \tag{15}$$

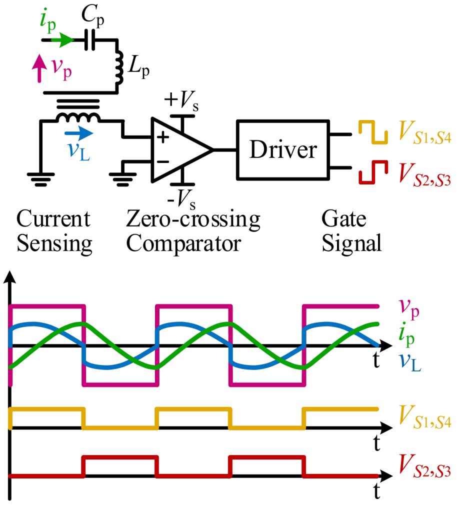

Fig. 7. Composition of the detection hardware circuit to generate the inverter gate signal and the relevant waveforms.

where

$$R_{\text{in}} = R_{\text{p}} + \frac{(\omega M)^2}{(R_{\text{s}} + R_{\text{eq}})^2 + {X_{\text{s}}}^2}(R_{\text{s}} + R_{\text{eq}}) \tag{16}$$

$$X_{\text{in}} = X_{\text{p}} - \frac{(\omega M)^2}{(R_{\text{s}} + R_{\text{eq}})^2 + {X_{\text{s}}}^2}(X_{\text{s}}) . \tag{17}$$

Additionally, the primary side RMS current I_{p} can be found using

$$I_{\text{p}} = \frac{V_{\text{p}}}{|R_{\text{in}} + jX_{\text{in}}|}. \tag{18}$$

The changes in I_{p} and $\cos(\theta)$ are examined from theoretical and simulation results shown in Fig. 6(a) and (b), which demonstrate the compensating effect against the coupling and load variations for maintaining approximate power in Fig. 6(c).

Based on the analysis of the dynamic behavior of the system, a brief qualitative explanation is as follows. When the coupling coefficient increases, it results in reduced I_{p} and θ as the inverter switches at lower peak current instants because the reflected impedance $Z_{\text{ref}} = (\omega M)^2/(Z_{\text{s}})$ increases. The switching frequency also increases due to earlier switching. As a result, the increase in the coupling coefficient causes I_{p} to decrease and $\cos(\theta)$ to increase, generating a compensating effect. It can be shown that a change in load has a similar effect to maintain the input power to be approximately constant. As shown in Fig. 5(c), efficiency variation range of the proposed system is relatively small, so an approximate constant input power indicates an approximate CP flow to the load.

III. Practical Design

This article implements the proposed AVFI system with constant power (CP) as an alternative to the conventional constant current (CC) stage, which covers most of the charging process in terms of the state of charge of a battery. CP can enhance charging speed and battery health [4] by maximizing the power transfer capability of the charger, thus reducing the overall charging duration [5]. The proposed AVFI IPT system is designed for a nominal 65 W output to charge a 36 V lithium-ion battery.

TABLE II
Key Experimental Setup Parameters

Symbol	Parameter	Value
V_{dc}	DC source voltage	60 V
f	Inverter frequency	100~200 kHz
k	Coupling coefficient	0.2 − 0.6
R_L	Load resistance	14 − 26 Ω
L_p	Primary coil inductance	41.33 μH
L_s	Secondary coil inductance	41.32 μH
C_p	Primary resonant capacitor	61.54 nF
C_s	Secondary resonant capacitor	61.63 nF
R_p	Primary coil ESR	0.11 Ω
R_s	Secondary coil ESR	0.11 Ω
V_{nom}	Nominal output voltage	36 V
P_{nom}	Nominal output power	65 W
k_{nom}	Nominal coupling coefficient	0.4
R_{nom}	Nominal load resistance	20 Ω

The system parameters in Table II fall within the <200 W power class and the 90–205 kHz frequency band, complying with the European Telecommunications Standards Institute standard [29], whose applications include robots and drones. The coil inductance values align with those reported in the literature for similar applications [15], [30], [31].

A. Nominal Operating Point

The implemented system is designed to deliver 65 W to a 36 V nominal lithium-ion battery. Lithium-ion batteries can exhibit a voltage variation of ±15% around the nominal value due to factors such as state of charge, temperature, and charge/discharge rate, resulting in a voltage range of approximately 30 to 42 V [32]. At 65 W, this corresponds to an equivalent resistive load of about 14 to 26 Ω. For a battery at 36 V nominal delivering 65 W, the equivalent resistive load is 20 Ω, which has been selected as the nominal load. A nominal coupling coefficient of 0.4 is chosen as it represents the midpoint of the 0.2 to 0.6 range, which aligns with the Qi standard [33]. Practically, the coupling and load variations may exceed the intended design specifications. Therefore, a robustness assessment of the proposed AVFI is provided in the Appendix.

B. Sensing Circuit

As discussed in Section II, the proposed AVFI operates by switching at the zero-crossing of the induced voltage from the Tx current, which aligns with the peak of the primary current i_{p}. The specific implementation of the detection hardware is shown in Fig. 7, along with the relevant waveforms. A ferrite toroid (Fair-Rite 61) is used, with the primary coil passing through the center of the toroid, while the sensing coil consists of four turns wound on the toroid. The induced voltage across the sensing coil is then fed into a zero-crossing comparator (TLV3501) whose output signal is connected to a gate driver (SI82394) to generate the gate

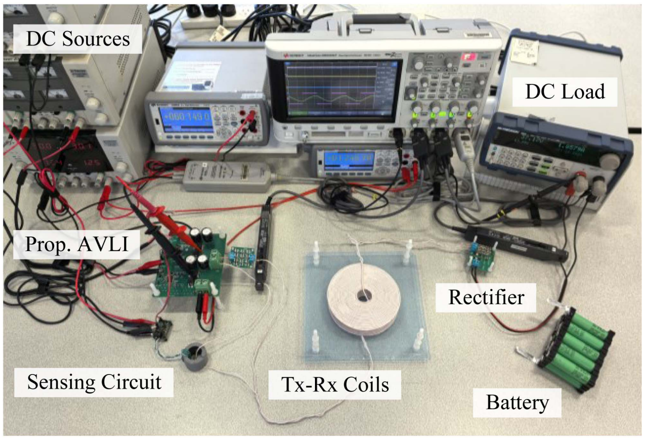

Fig. 8. Experimental setup of the proposed system.

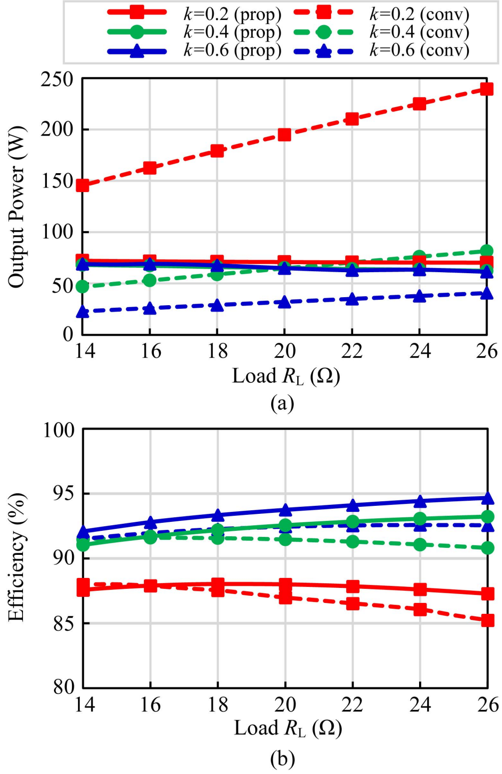

Fig. 9. Comparison of proposed against conventional system across a range of load R_L and k. (a) Output power. (b) System efficiency.

signals $V_{g1,2}$ for the inverter. Due to the nature of inductors, in the time domain, the voltage across the sensing coil is proportional to the derivative of the primary current ($v_L = L*di/dt$). This relationship ensures that the voltage becomes zero when the primary current i_p reaches its peak, thereby ensuring the inverter switches at peak primary current.

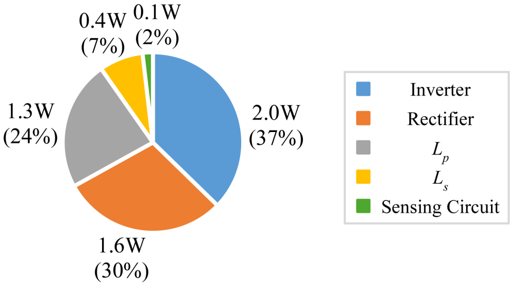

Fig. 10. Power loss of the proposed system at the nominal operating point ($P_{\mathrm{out}} = 65$ W, $R_L = 20\ \Omega$, $k = 0.4$).

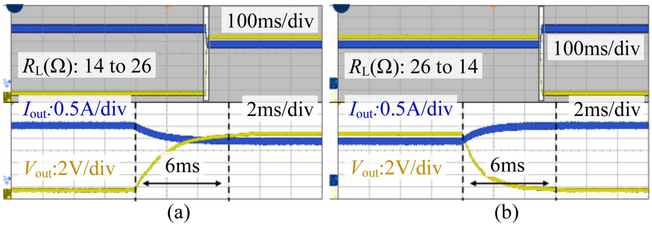

(a) (b)

Fig. 11. Measured waveforms at nominal k of 0.4, when the load R_L changes from: (a) 14 to 26 Ω and (b) 26 to 14 Ω.

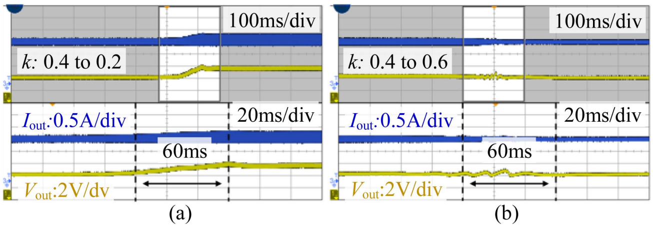

(a) (b)

Fig. 12. Measured waveforms at nominal 20 Ω load, when the coupling coefficient k changes from: (a) 0.4 to 0.2 and (b) 0.4 to 0.6.

IV. EXPERIMENTAL RESULTS

An experimental prototype has been built to verify the proposed AVFI system, as shown in Fig. 8. The system parameters are presented in Table II. The primary and secondary coils each have 26 turns, with an inner diameter of 25 mm and an outer diameter of 121.5 mm. The Litz-wire used has a total diameter of 1.5 mm and consists of 330 strands of AWG41. The full bridge inverter uses the gate driver (SI82394) to drive the MOSFET (IPB073N15N5ATMA1). Schottky diode (MBR12U100L) is used to form the full bridge rectifier. A programmable dc electronic load (BK Precision 8602) is employed as an adjustable equivalent load R_L. The battery pack consists of ten lithium-ion cells (Samsung INR18650-25R) connected in series, providing a nominal voltage of 36 V. Signal waveforms and system performance are analyzed using an oscilloscope (Keysight MSOX3034T) with a differential voltage probe (Keysight N2790A), a current probe (HIOKI 3276) and a multimeter (Keysight 34465A).

A. Output Power and Efficiency

Fig. 9 compares the output power and dc–dc efficiency of the proposed and conventional systems, with the latter included to highlight the performance of the proposed system. The only

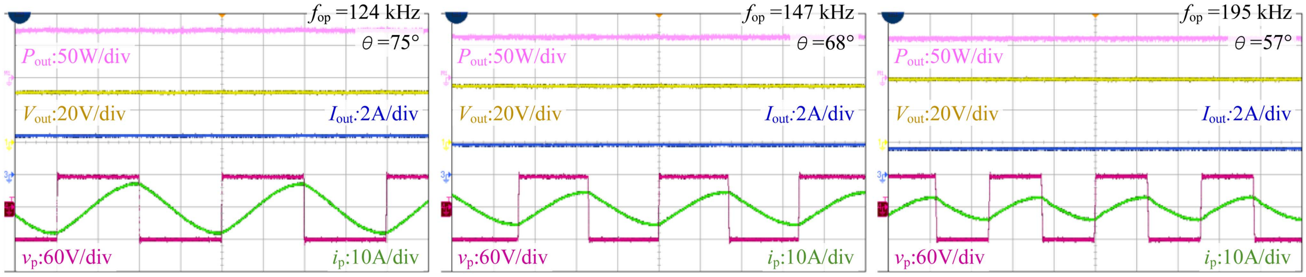

k=0.2, R_L=14Ω k=0.4, R_L=20Ω k=0.6, R_L=26Ω

Fig. 13. Measured steady-state waveforms of the proposed AVFI with a resistive load at various coupling coefficient k and load R_L conditions.

differences between the two systems are the operating frequency and the dc input voltage. In the conventional system, an external function generator supplies a fixed 100 kHz gate signal to the inverter, as both systems are tuned to a 100 kHz resonance frequency, which falls under the Qi standard [33]. Because the proposed system achieves CP at a fixed input dc voltage (V_{dc}), both systems are operated at a fixed V_{dc} for fair comparison, chosen to achieve a nominal operating point of 36 V and 65 W output power, with a coupling coefficient of 0.4 at a load of 20 Ω. This results in V_{dc} values of 60 V for the proposed system and 24 V for the conventional system. All other parameters follow Table II.

Fig. 9(a) shows that the output power of the proposed AVFI is near constant even when R_L and k change, which matches the theoretical explanation in Section II. The output power of the proposed AVFI system at a nominal 20 Ω is 71, 65, and 64 W for coupling coefficients of 0.2, 0.4, and 0.6, respectively. The proposed AVFI system achieves quasi CP at the nominal 65 W, with a 10.8% deviation at most. In contrast, the conventional system shows output power values of 195, 65, and 32 W at the same nominal load and coupling coefficients, revealing that it does not achieve quasi CP and exhibits deviations of up to 267.7%.

Fig. 9(b) shows the efficiency comparison. The proposed AVFI system exhibits efficiency comparable to that of the conventional system. At a nominal 20 Ω load, the proposed system achieves efficiencies of 88%, 92%, and 94% for coupling coefficients of 0.2, 0.4, and 0.6, respectively, maintaining an overall efficiency range of 87% to 95%. In comparison, the conventional system achieves efficiencies of 87%, 91%, and 92% under the same conditions, with an overall range of 85% to 93%. Fig. 10 depicts the power loss distribution of the proposed system at the nominal operating point. ($P_{out} = 65$ *W*, $R_L = 20$ Ω, $k = 0.4$).

B. Dynamic Response

Fig. 11 shows the dynamic response to a step load change at a nominal coupling coefficient k of 0.4. In Fig. 11(a), the load steps from 14 to 26 Ω causing voltage V_{out} to increase from 30.8 to 40.2 V, and the current I_{out} to decrease from 2.2 to 1.5 A, with a response time of 6 ms. Fig. 11(b) shows the load stepping from 26 to 14 Ω, reversing these changes, again taking 6 ms.

Fig. 12 shows the dynamic response to changes in coupling k at a nominal load of 20 Ω. In Fig. 12(a), the coupling k decreases from 0.4 to 0.2, causing the voltage V_{out} to change from 36.5 to 37.7 V, and the current I_{out} changes from 1.82 to 1.88 A, with a dynamic response of 60 ms. In Fig. 12(b), the coupling k increases from 0.4 to 0.6. The voltage V_{out} changes from 36.5 to 36.2 V, and the current I_{out} changes from 1.82 to 1.80 A, with a dynamic response of 60 ms.

C. Steady-State Waveforms and Zero Voltage Switching

Fig. 13 illustrates the inverter output voltage v_p, the primary current i_p of the proposed AVFI, and the output power P_{out} and voltage V_{out} of the resistive load under various coupling coefficients and load conditions. As shown in Fig. 13, the AVFI automatically adjusts its operating frequency, which also results in varying current i_p magnitude and phase between the inverter voltage v_p and current i_p to achieve quasi constant output power. This behavior matches the theoretical analysis in Section II, confirming the self-regulating mechanism of the AVFI.

Furthermore, Fig. 13 shows that the voltage v_p leads the primary current i_p, demonstrating that the impedance of the inverter is inductive. This inductive behavior causes the current through the switch to initially flow negatively, discharging the parasitic output capacitance and enabling zero-voltage switching in the full-bridge inverter [34].

D. Performance With a Battery Load

To evaluate the performance of the proposed AVFI on charging a battery directly, the dc electronic load is replaced with a nominal 36 V lithium-ion battery pack. Fig. 14 shows the steady-state waveforms of the inverter output voltage v_p and primary current i_p, along with the output power and battery voltage under different coupling coefficients and load conditions. At the nominal output of 65 W, the equivalent resistive load corresponds to about 14, 20, and 26 Ω for battery voltages of 30, 36, and 42 V, respectively. These operating points demonstrate consistency between the waveforms in Figs. 13 and 14.

Fig. 15 presents the battery charging power and voltage over time under different coupling coefficients. In this experiment, charging starts at 30 V and ends when the battery voltage reaches 42 V. The proposed AVFI system achieving quasi CP serves as an alternative to the conventional CC stage.

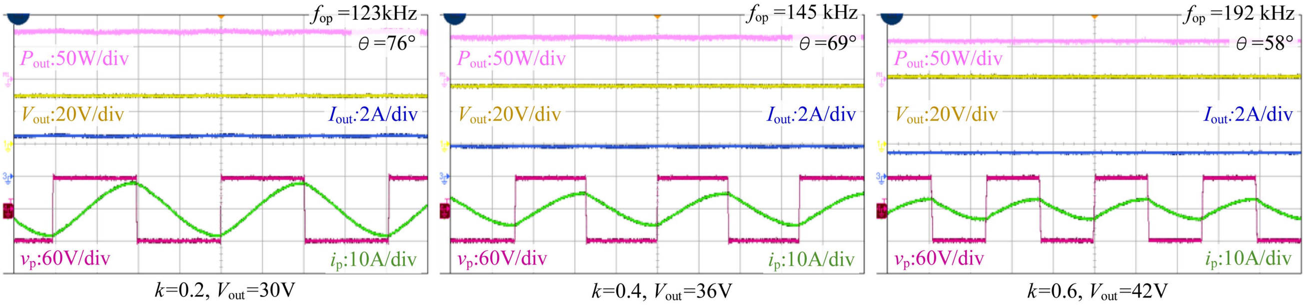

k=0.2, V_{out}=30V k=0.4, V_{out}=36V k=0.6, V_{out}=42V

Fig. 14. Measured steady-state waveforms of the proposed AVFI with a battery load at various coupling coefficient k and voltage $\mathrm{V}_{\mathrm{out}}$ conditions.

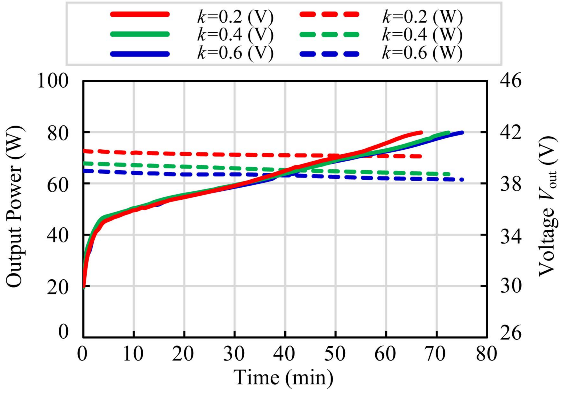

Fig. 15. Output power and voltage of the battery load at different coupling coefficient.

V. CONCLUSION

This article proposed a communication free autonomous voltage-fed inverter (AVFI) IPT system capable of achieving quasi constant output power against magnetic coupling and load variations. The proposed method eliminates the need for additional dc–dc converters and complex control. Theoretical analysis and experimental validation have been conducted to validate the proposed system. Experimental results show that the proposed system delivers quasi constant output power when the coupling coefficient varies from 0.2 to 0.6 and the load is changed from 14 to 26 Ω. Furthermore, the proposed AVFI achieves zero voltage switching operation.

APPENDIX

A. Derivation of Primary and Secondary Current Time-Domain Expressions

The time domain expression under a step response for primary current $i_{\mathrm{p}}(t)$ and secondary current $i_{\mathrm{s}}(t)$ are obtained using mathematical tools such as MATLAB and Mathematica to perform the inverse Laplace transform on (6) and (7), leading to expressions (A1) and (A2) shown at the top of the next page. These equations were used to analyze the steady-state operation of the system, including the operating frequency, using the method proposed in Section II-A. To simplify these expressions, a root term λ_k and a denominator term $D(\lambda_k)$ (A3) shown at the top of the next page is defined consistently across all terms.

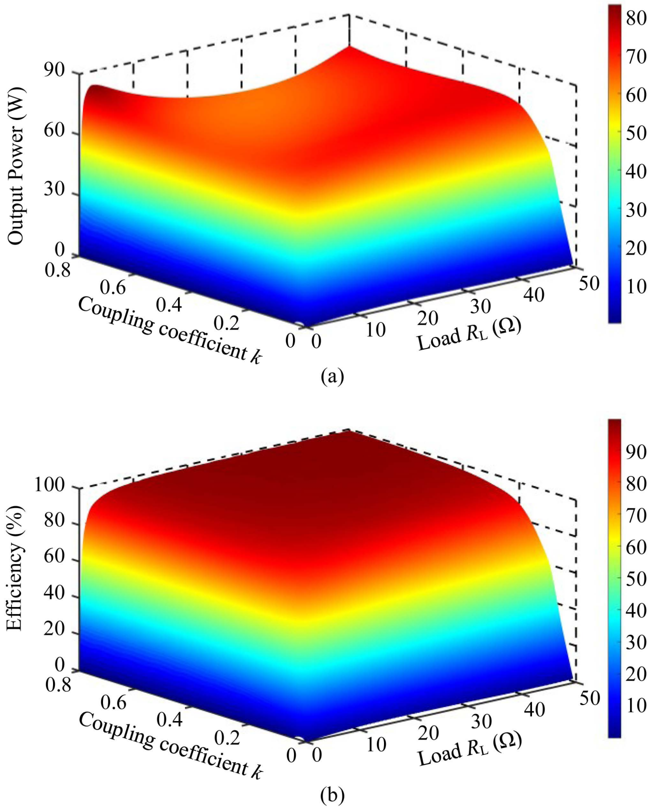

(a)

(b)

Fig. 16. Characteristics of the proposed system against coupling coefficient k and load R_{L}. (a) Output power. (b) Transfer efficiency.

B. Output Power and Efficiency Under Extreme Conditions

Applying the method presented in Section II, the proposed AVFI system is analyzed across a wider range of coupling and load variations, as shown in Fig. 16. The system achieves quasi CP within a centralized region. However, as the coupling and load vary significantly, the output power deviates from being quasi constant.

$$\begin{aligned} i_{\mathrm{p}}(t) = {} & C_{\mathrm{p}}V_{dc}\sum_{k=1}^{4}\frac{e^{t\lambda_k}}{D\left(\lambda_k\right)} - C_{\mathrm{p}}V_{Cp,0}\sum_{k=1}^{4}\frac{e^{t\lambda_k}}{D\left(\lambda_k\right)} + C_{\mathrm{p}}I_{\mathrm{p},0}L_{\mathrm{p}}\sum_{k=1}^{4}\frac{\lambda_k e^{t\lambda_k}}{D\left(\lambda_k\right)} + C_{\mathrm{p}}I_{\mathrm{s},0}M\sum_{k=1}^{4}\frac{\lambda_k e^{t\lambda_k}}{D\left(\lambda_k\right)} - C_{\mathrm{p}}C_{\mathrm{s}}I_{\mathrm{p},0}M^2\sum_{k=1}^{4}\frac{\lambda_k^3 e^{t\lambda_k}}{D\left(\lambda_k\right)} \\ & + C_{\mathrm{p}}C_{\mathrm{s}}R_{\mathrm{s}}V_0\sum_{k=1}^{4}\frac{\lambda_k e^{t\lambda_k}}{D\left(\lambda_k\right)} - C_{\mathrm{p}}C_{\mathrm{s}}R_{\mathrm{s}}V_{\mathrm{C}s,0}\sum_{k=1}^{4}\frac{\lambda_k e^{t\lambda_k}}{D\left(\lambda_k\right)} + C_{\mathrm{p}}C_{\mathrm{s}}L_{\mathrm{s}}V_{dc}\sum_{k=1}^{4}\frac{\lambda_k^2 e^{t\lambda_k}}{D\left(\lambda_k\right)} - C_{\mathrm{p}}C_{\mathrm{s}}L_{\mathrm{s}}V_{Cp,0}\sum_{k=1}^{4}\frac{\lambda_k^2 e^{t\lambda_k}}{D\left(\lambda_k\right)} \\ & + C_{\mathrm{p}}C_{\mathrm{s}}MV_{Cs,0}\sum_{k=1}^{4}\frac{\lambda_k^2 e^{t\lambda_k}}{D\left(\lambda_k\right)} + C_{\mathrm{p}}C_{\mathrm{s}}I_{\mathrm{p},0}L_{\mathrm{p}}L_{\mathrm{s}}\sum_{k=1}^{4}\frac{\lambda_k^3 e^{t\lambda_k}}{D\left(\lambda_k\right)} + C_{\mathrm{p}}C_{\mathrm{s}}I_{\mathrm{p},0}L_{\mathrm{p}}R_{\mathrm{s}}\sum_{k=1}^{4}\frac{\lambda_k^2 e^{t\lambda_k}}{D\left(\lambda_k\right)} + C_{\mathrm{p}}C_{\mathrm{s}}I_{\mathrm{s},0}MR_{\mathrm{s}}\sum_{k=1}^{4}\frac{\lambda_k^2 e^{t\lambda_k}}{D\left(\lambda_k\right)} \end{aligned} \tag{A1}$$

$$\begin{aligned} i_{\mathrm{s}}(t) = {} & -C_{\mathrm{s}}V_{Cs,0}\sum_{k=1}^{4}\frac{e^{t\lambda_k}}{D\left(\lambda_k\right)} + C_{\mathrm{s}}I_{\mathrm{s},0}L_{\mathrm{s}}\sum_{k=1}^{4}\frac{\lambda_k e^{t\lambda_k}}{D\left(\lambda_k\right)} + C_{\mathrm{s}}I_{\mathrm{p},0}M\sum_{k=1}^{4}\frac{\lambda_k e^{t\lambda_k}}{D\left(\lambda_k\right)} - C_{\mathrm{p}}C_{\mathrm{s}}I_{\mathrm{s},0}M^2\sum_{k=1}^{4}\frac{\lambda_k^3 e^{t\lambda_k}}{D\left(\lambda_k\right)} \\ & - C_{\mathrm{p}}C_{\mathrm{s}}R_{\mathrm{p}}V_{Cs,0}\sum_{k=1}^{4}\frac{\lambda_k e^{t\lambda_k}}{D\left(\lambda_k\right)} - C_{\mathrm{p}}C_{\mathrm{s}}L_{\mathrm{p}}V_{Cs,0}\sum_{k=1}^{4}\frac{\lambda_k^2 e^{t\lambda_k}}{D\left(\lambda_k\right)} + C_{\mathrm{p}}C_{\mathrm{s}}I_{\mathrm{s},0}L_{\mathrm{p}}L_{\mathrm{s}}\sum_{k=1}^{4}\frac{\lambda_k^3 e^{t\lambda_k}}{D\left(\lambda_k\right)} + C_{\mathrm{p}}C_{\mathrm{s}}I_{\mathrm{s},0}L_{\mathrm{s}}R_{\mathrm{p}}\sum_{k=1}^{4}\frac{\lambda_k^2 e^{t\lambda_k}}{D\left(\lambda_k\right)} \\ & + C_{\mathrm{p}}C_{\mathrm{s}}I_{\mathrm{p},0}MR_{\mathrm{p}}\sum_{k=1}^{4}\frac{\lambda_k^2 e^{t\lambda_k}}{D\left(\lambda_k\right)} - C_{\mathrm{p}}C_{\mathrm{s}}MV_{dc}\sum_{k=1}^{4}\frac{\lambda_k^2 e^{t\lambda_k}}{D\left(\lambda_k\right)} + C_{\mathrm{p}}C_{\mathrm{s}}MV_{Cp,0}\sum_{k=1}^{4}\frac{\lambda_k^2 e^{t\lambda_k}}{D\left(\lambda_k\right)} \end{aligned} \tag{A2}$$

where

$$\begin{cases} \lambda_k = \\ \sqrt[4]{C_{\mathrm{p}}C_{\mathrm{s}}M^2z^4 - C_{\mathrm{p}}C_{\mathrm{s}}L_{\mathrm{p}}L_{\mathrm{s}}z^4 - C_{\mathrm{p}}C_{\mathrm{s}}L_{\mathrm{s}}R_{\mathrm{p}}z^3 - C_{\mathrm{p}}C_{\mathrm{s}}L_{\mathrm{p}}R_{\mathrm{s}}z^3 - C_{\mathrm{p}}C_{\mathrm{s}}R_{\mathrm{p}}R_{\mathrm{s}}z^2 - C_{\mathrm{s}}L_{\mathrm{s}}z^2 - C_{\mathrm{p}}L_{\mathrm{p}}z^2 - C_{\mathrm{s}}R_{\mathrm{s}}z - C_{\mathrm{p}}R_{\mathrm{p}}z - 1} \\ D\left(\lambda_k\right) = \\ C_{\mathrm{p}}R_{\mathrm{p}} + C_{\mathrm{s}}R_{\mathrm{s}} + 2C_{\mathrm{p}}L_{\mathrm{p}}\lambda_k + 2C_{\mathrm{s}}L_{\mathrm{s}}\lambda_k - 4C_{\mathrm{p}}C_{\mathrm{s}}M^2\lambda_k^3 + 2C_{\mathrm{p}}C_{\mathrm{s}}R_{\mathrm{p}}R_{\mathrm{s}}\lambda_k + 4C_{\mathrm{p}}C_{\mathrm{s}}L_{\mathrm{p}}L_{\mathrm{s}}\lambda_k^3 + 3C_{\mathrm{p}}C_{\mathrm{s}}L_{\mathrm{p}}R_{\mathrm{s}}\lambda_k^2 + 3C_{\mathrm{p}}C_{\mathrm{s}}L_{\mathrm{s}}R_{\mathrm{p}}\lambda_k^2 \end{cases} . \tag{A3}$$

REFERENCES

[1] P. K. Chittoor, B. Chokkalingam, and L. Mihet-Popa, "A review on UAV wireless charging: Fundamentals, applications, charging techniques and standards," *IEEE Access*, vol. 9, pp. 69235–69266, 2021.

[2] C. Zhu et al., "Analysis and design of cost-effective WPT systems with dual independently regulatable outputs for automatic guided vehicles," *IEEE Trans. Power Electron.*, vol. 36, no. 6, pp. 6183–6187, Jun. 2021.

[3] Z. Huang, G. Wang, J. Yu, and X. Qu, "A novel clamp coil assisted IPT battery charger with inherent CC-to-CV transition capability," *IEEE Trans. Power Electron.*, vol. 36, no. 8, pp. 8607–8611, Aug. 2021.

[4] S. S. Zhang, "The effect of the charging protocol on the cycle life of a Li-ion battery," *J. Power Sources*, vol. 161, no. 2, pp. 1385–1391, Oct. 2006.

[5] Z. Li, H. Liu, Y. Huo, J. He, Y. Tian, and J. Liu, "High-misalignment tolerance wireless charging system for constant power output using dual transmission channels with magnetic flux controlled inductors," *IEEE Trans. Power Electron.*, vol. 37, no. 11, pp. 13930–13945, Nov. 2022.

[6] N. K. Poon, B. M. H. Pong, and C. K. Tse, "A constant-power battery charger with inherent soft switching and power factor correction," *IEEE Trans. Power Electron.*, vol. 18, no. 6, pp. 1262–1269, Nov. 2003.

[7] D. A. Zambrano-Prada, A. El Aroudi, O. López-Santos, L. Vázquez-Seisdedos, and L. Martínez-Salamero, "Constant power-constant voltage battery charging based on a loss-free resistor approach," *IEEE Trans. Circuits Syst. I, Reg. Papers*, vol. 71, no. 10, pp. 4778–4791, Oct. 2024.

[8] J. Zhou, B. Zhang, W. Xiao, D. Qiu, and Y. Chen, "Nonlinear parity-time-symmetric model for constant efficiency wireless power transfer: Application to a drone-in-flight wireless charging platform," *IEEE Trans. Ind. Electron.*, vol. 66, no. 5, pp. 4097–4107, May 2019.

[9] Y. Gu, J. Wang, Z. Liang, and Z. Zhang, "Flexible constant-power range extension of self-oscillating system for wireless In-flight charging of drones," *IEEE Trans. Power Electron.*, vol. 39, no. 11, pp. 15342–15355, Nov. 2024.

[10] F. Xu, S. -C. Wong, and C. K. Tse, "Overall loss compensation and optimization control in single-stage inductive power transfer converter delivering constant power," *IEEE Trans. Power Electron.*, vol. 37, no. 1, pp. 1146–1158, Jan. 2022.

[11] Z. Luo, Y. Zhao, M. Xiong, X. Wei, and H. Dai, "A self-tuning LCC/LCC system based on switch-controlled capacitors for constant-power wireless electric vehicle charging," *IEEE Trans. Ind. Electron.*, vol. 70, no. 1, pp. 709–720, Jan. 2023.

[12] Z. Huang et al., "A single-stage inductive-power-transfer converter for constant-power and maximum-efficiency battery charging," *IEEE Trans. Power Electron.*, vol. 35, no. 9, pp. 8973–8984, Sep. 2020.

[13] B. Zou and Z. Huang, "Primary-frequency-tuning and secondary-impedance-matching IPT converter with programmable constant power output and optimal efficiency tracking against variation of coupling coefficient," *IEEE Trans. Power Electron.*, vol. 39, no. 4, pp. 4895–4909, Apr. 2024.

[14] I. -W. Iam, C. -K. Choi, C. -S. Lam, P. -I. Mak, and R. P. Martins, "A constant-power and optimal-transfer-efficiency wireless inductive power transfer converter for battery charger," *IEEE Trans. Ind. Electron.*, vol. 71, no. 1, pp. 450–461, Jan. 2024.

[15] J. Zeng, J. Wu, K. Li, Y. Yang, and S. Y. R. Hui, "Dynamic monitoring of battery variables and mutual inductance for primary-side control of a wireless charging system," *IEEE Trans. Ind. Electron.*, vol. 71, no. 7, pp. 7966–7974, Jul. 2024.

[16] J. Zeng, Y. Yang, K. Li, S. Chen, and S. Y. R. Hui, "An ultrafast estimation method for coupling coefficient and receiver resonant frequency in universal wireless power transfer systems," *IEEE Trans. Power Electron.*, vol. 39, no. 4, pp. 4870–4883, Apr. 2024.

[17] Y. Yang, S. -C. Tan, and S. Y. R. Hui, "Front-end parameter monitoring method based on two-layer adaptive differential evolution for SS-compensated wireless power transfer systems," *IEEE Trans. Ind. Informat.*, vol. 15, no. 11, pp. 6101–6113, Nov. 2019.

[18] R. Dai, W. Zhou, Y. Chen, Z. Zhu, and R. Mai, "Pulse density modulation based mutual inductance and load resistance identification method for wireless power transfer system," *IEEE Trans. Power Electron.*, vol. 37, no. 8, pp. 9933–9943, Aug. 2022.

[19] Y. -G. Su, H. -Y. Zhang, Z. -H. Wang, A. P. Hu, L. Chen, and Y. Sun, "Steady-State load identification method of inductive power transfer system based on switching capacitors," *IEEE Trans. Power Electron.*, vol. 30, no. 11, pp. 6349–6355, Nov. 2015.

[20] L. Wu, B. Zhang, Y. Jiang, and J. Zhou, "A robust parity-time-symmetric WPT system with extended constant-power range for cordless kitchen appliances," *IEEE Trans. Ind. Appl.*, vol. 58, no. 1, pp. 1179–1189, Jan. 2022.

[21] X. Shu, B. Zhang, Z. Wei, C. Rong, and S. Sun, "Extended-distance wireless power transfer system with constant output power and transfer efficiency based on parity-time-symmetric principle," *IEEE Trans. Power Electron.*, vol. 36, no. 8, pp. 8861–8871, Aug. 2021.

[22] H. Zhu, B. Zhang, and L. Wu, "Output power stabilization for wireless power transfer system employing primary-side-only control," *IEEE Access*, vol. 8, pp. 63735–63747, 2020.

[23] Y. Gu, J. Wang, Z. Liang, and Z. Zhang, "Communication-free power control algorithm for drone wireless in-flight charging under dual-disturbance of mutual inductance and load," *IEEE Trans. Ind. Inform.*, vol. 20, no. 3, pp. 3703–3714, Mar. 2024.

[24] K. Yan, Q. Chen, J. Hou, X. Ren, and X. Ruan, "Self-oscillating contactless resonant converter with phase detection contactless current transformer," *IEEE Trans. Power Electron.*, vol. 29, no. 8, pp. 4438–4449, Aug. 2014.

[25] L. Xu, Q. Chen, X. Ren, S. -C. Wong, and C. K. Tse, "Self-oscillating resonant converter with contactless power transfer and integrated current sensing transformer," *IEEE Trans. Power Electron.*, vol. 32, no. 6, pp. 4839–4851, Jun. 2017.

[26] D. Ahn and S. Hong, "Wireless power transmission with self-regulated output voltage for biomedical implant," *IEEE Trans. Ind. Electron.*, vol. 61, no. 5, pp. 2225–2235, May 2014.

[27] W. Zhong and S. Y. R. Hui, "Maximum energy efficiency operation of series-series resonant wireless power transfer systems using on-off keying modulation," *IEEE Trans. Power Electron.*, vol. 33, no. 4, pp. 3595–3603, Apr. 2018.

[28] J. Wu, K. Li, J. Zeng, and S.-Y. R. Hui, "On the limitations of the coupled mode theory and parity-time symmetry for near-field wireless power transfer research," *IEEE Trans. Power Electron.*, vol. 39, no. 5, pp. 6433–6441, May 2024.

[29] *System Reference Document (SRdoc); Wireless Power Transmission (WPT) Systems Operating Below 30 MHz*, ETSI TR 103 493 V1.1.1, Feb. 2019.

[30] E. S. Lee, "Frequency-modulation-based IPT with magnetic communication for EV wireless charging," *IEEE Trans. Ind. Electron.*, vol. 70, no. 2, pp. 1398–1408, Feb. 2023.

[31] X. Li, H. Wang, F. Zheng, X. Dai, Y. Sun, and A. P. Hu, "Wireless charging of substation inspection robots based on parameter estimation without communication," *IEEE Trans. Circuits Syst. II, Exp. Briefs*, vol. 71, no. 2, pp. 907–911, Feb. 2024.

[32] L. Gao, S. Liu, and R. A. Dougal, "Dynamic lithium-ion battery model for system simulation," *IEEE Trans. Compon. Packag. Technol.*, vol. 25, no. 3, pp. 495–505, Sep. 2002.

[33] Wireless Power Consortium Website, Accessed: Dec. 18, 2024. [Online]. Available: https://www.wirelesspowerconsortium.com

[34] J. Zhou, C. Q. Jiang, T. Ma, G. Guidi, X. Zhang, and J. A. Suul, "Comprehensive analysis of bifurcation and frequency splitting phenomena in inductive battery charging systems," *IEEE Trans. Power Electron.*, vol. 39, no. 11, pp. 15329–15341, Nov. 2024.

Aoyang Laurence Li (Student Member, IEEE) received the B.E. (Hons.) degree in electrical and electronics engineering in 2024 from the University of Auckland, Auckland, New Zealand, where he is currently working toward the Ph.D. degree.

His research interests include wireless power transfer for low power devices, and power electronics.

Mingdong Edward Han (Student Member, IEEE) received the B.E. (Hons.) and B.Com. conjoint degree in 2017 from the University of Auckland, Auckland, New Zealand, where he is currently working toward the Ph.D. degree in electrical and electronics engineering.

His research interests include wireless power transfer and power electronics.

Saidul Alam Chowdhury received the B.S. degree in electrical and electronic engineering from Chittagong University of Engineering and Technology, Chittagong, Bangladesh, in 2017, and the M.S. and Ph.D. degrees in electrical engineering from Incheon National University, Incheon, South Korea, in 2021 and 2024, respectively.

Since March 2024, he has been a Postdoctoral Research Fellow with the Department of Electrical, Computer and Software Engineering, University of Auckland, Auckland, New Zealand. His current research interests include power electronics for wireless power transfer, power converters, and analog/RF integrated circuit design.

Aiguo Patrick Hu (Senior Member, IEEE) received the B.E. and M.E. degrees in electrical engineering from Xi'an Jiaotong University, Xi'an, China, in 1985 and 1988, respectively, and the Ph.D. degree in electrical engineering from The University of Auckland, Auckland, New Zealand, in 2001.

He stayed with the National University of Singapore, Singapore, for a semester as an Exchange Postdoctoral Research Fellow. He has authored more than 200 peer-reviewed journal and conference articles with about 4500 citations, authored the first monograph on inductive power transfer technology, and contributed 4 book chapters on wireless power transfer modeling and control, as well as electrical machines. He is currently a Full Professor with the Department of Electrical and Electronic Engineering, University of Auckland. His research interests include wireless/contactless power transfer systems and application of power electronics in renewable energy systems.

Dr. Hu was a recipient of the University of Auckland VC's Funded Research and Commercialization Medal in April 2017.